# Hindered Nanoparticle Diffusion and Void Accessibility in a Three-Dimensional Porous Medium

Michael J. Skaug,[†,⊥] Liang Wang,[‡] Yifu Ding,[‡,§] and Daniel K. Schwartz[*,†,§]

[†]Department of Chemical and Biological Engineering, [‡]Department of Mechanical Engineering, and [§]Materials Science and Engineering Program, University of Colorado Boulder, Boulder, Colorado 80309, United States. [⊥]Present address (for M.J.S.): IBM Research—Zurich, 8803 Rüschlikon, Switzerland.

ABSTRACT The inherent pore-scale heterogeneity of many natural and synthetic porous materials can make it difficult to model and predict porous transport because the underlying microscopic processes are often poorly understood. Here we present the results of single-particle tracking experiments in which we followed the pore-scale diffusion of individual nanoparticles, deep within a three-dimensional porous material of moderate porosity. We observed significant hydrodynamic damping of particle motion at subpore length scales, resulting in heterogeneous and spatially dependent mobility. The accessibility of the void space was strongly dependent on particle size, and related to the heterogeneous hydrodynamics. Our results suggest that pore-scale diffusion is more heterogeneous and volume accessibility more limited than previously expected. The method demonstrated here will enable studies of a broad new class of materials including porous polymers of technological interest.
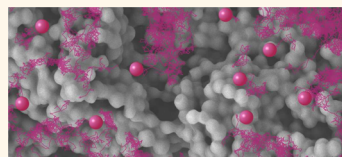
KEYWORDS: porous media · diffusion · nanoparticle · transport · single-particle tracking · fluorescence

From the fissured stone underground to the engineered membranes used to separate chemicals, porous materials are found throughout nature and technology. The solid porous matrix imposes barriers to diffusion within the void space. In some cases, like filtration membranes[1] and size-exclusion chromatography,[2] hindered transport is required for technological function. In other cases, like porous tissue scaffolds,[3,4] treatment of tumors[5] and resource extraction,[6,7] slow transport through the porous network may be undesirable.

Whether or not it is beneficial, hindered diffusion within porous materials is critical to many phenomena and applications, but we have an incomplete understanding of the microscopic processes that combine to produce the macroscopically observed transport. Most theoretical models used to describe porous diffusion, start with a microscopic description of particle dynamics at the length scale of a single pore.[8–13] The dynamics are then averaged over the heterogeneous porous structure to arrive at the macroscopic transport properties. However, most experimental efforts have focused on the dynamics over length scales larger than a single pore or measured ensemble behavior, where the microscopic

mechanisms that gave rise to porous transport are obscured.[14–19] This has made it difficult to determine the underlying origin of the frequently observed anomalous diffusion in heterogeneous environments, particularly in in biological systems.[20–23]

Pore-scale dynamics are particularly important when chemical reactions take place within the confines of the porous medium.[24,25] For heterogeneous catalysts and biological systems, pore-level details can influence reactions and signaling events by modifying the statistics of the underlying search process. Significant progress has been made in describing the statistical properties of complex diffusion processes,[26] particularly in their application to biological systems.[27] Predictions have also been made for how confinement geometry can influence mass transport in unexpected ways.[28,29] With a deeper understanding of pore-scale diffusion, it may be possible to design more efficient catalysts and mass separators.

To uncover the microscopic mechanisms of porous transport, experiments are needed that track the motion of individual particles from subpore to macroscopic length scales. Pioneering work from the Brauchle group used single molecule trajectories to visualize

the heterogeneous structure and diffusive dynamics in porous silica.[30,31] Other experiments have focused on high porosity gel networks,[32,33] colloidal suspensions[34] or microfabricated models.[35,36] What has been missing are single-particle experiments in three-dimensional porous materials of moderate porosity that go beyond system specific behavior.

To address this need, we developed an experimental system that allows imaging of single particle motion deep (~20 μm) within a three-dimensional porous polymer film. Optical imaging of porous materials is difficult because refractive index differences between the voids and solid matrix refract light. In the past, this difficulty has been overcome by using either sub-wavelength pores (e.g., nanoporous glass[30]) or sub-wavelength solid matrix (e.g., gel networks[32,33]). The other solution is to permeate the voids with a liquid that has the same refractive index as the solid matrix. Until now, this index-matching technique has been restricted to solid matrices composed of fused silica[17,19] or poly(methyl methacrylate),[34] thus limiting the scope of technologically important porous materials that could be studied.

In the first part of this work, we present a method for index-matching a porous polymer material, which will enable imaging within a broad new class of materials. The method involves permeating the pores with a unique, polar and high refractive index liquid, thio-diethanol (TDE). The polarity, miscibility with water and high refractive index (n = 1.52) of TDE enables optical imaging within a variety of technologically relevant porous materials, including those often used in separation processes, like borosilicate glass ($n \sim 1.52$), poly(vinylidene fluoride) ($n \sim 1.42$), and nitrocellulose ($n \sim 1.50$), and biomaterial scaffolds, like poly(ethylene glycol) ($n \sim 1.46$) and poly(L-lactic acid) ($n \sim 1.46$).

We then present results of experiments imaging the diffusive motion of submicron fluorescent colloidal particles (40, 100, and 200 nm) within a porous polymer film of moderate porosity. The disordered network of $0.1-10$ μm pores and voids gave rise to heterogeneous, non-Gaussian and subdiffusive particle dynamics. Spatial maps of particle occupancy indicated surprisingly strong pore-exclusion effects, with larger particles being confined to a few large pores. The data also highlighted the significance of hydrodynamic interactions on the motion of confined particles: even at length scales much smaller than the pore size, particle motion was much slower than in the unconfined bulk liquid.

RESULTS

Tracking Particles in the Disordered Pore Space. In order to image particle motion microns deep in the porous polymer, it was necessary to fill the void space with a liquid of the same refractive index as the polymer matrix, n = 1.52. We required a liquid that (1) was
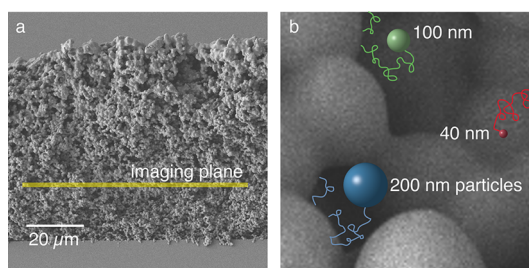

Figure 1. Imaging colloid motion in the void space of a porous film. (a) Scanning electron microscopy (SEM) image of the porous sample, showing the free surface, the surface in contact with the microscope coverglass and the approximate imaging plane. (b) A composite illustration showing a higher magnification image of the porous sample and the relative size of the fluorescent tracer particles.

transparent, (2) had a refractive index $n \sim 1.52$, and (3) did not swell or dissolve the solid matrix or tracer particles. The requirement that the liquid not swell the polymer matrix greatly reduced the number of candidate liquids because many liquids with a refractive index $n \sim 1.52$ are also nonpolar and good solvents for organic compounds. Thiodiethanol (TDE) met the above requirements; it has a refractive index of n = 1.52, it is sufficiently polar to make it miscible with water, and it is transparent.[37] To test the suitability of TDE with the polymer sample materials, we immersed a bulk NOA65 sample in TDE and found there to be no change in material properties after 1 week, and there was no evidence of fluorescence leaching from the polystyrene particles suspended in TDE for more than 3 months.

We permeated the void space of the porous polymer samples with TDE containing a dilute concentration of fluorescent colloidal particles (volume fraction $10^{-4} < \phi < 10^{-6}$ or number density $n \approx 10^9$/mL). The refractive index match between TDE and polymer matrix enabled the use of epifluorescence microscopy to track the motion of individual particles as they diffused within the voids near the midplane of the porous film (Figure 1). In initial experiments, we found that particles were completely immobilized within the voids, presumably adsorbed to the pore walls. Although transient binding to the pore walls may be valuable to study in future experiments, our goal in this work was to understand purely geometric obstruction effects, so we added 17% by volume of a nonionic detergent, Triton X-100, to the TDE permeating liquid, which mobilized the particles and only slightly decreased the refractive index of the liquid solution ($n \sim 1.51$). Plotting the accumulated two-dimensional particle trajectories revealed the underlying void space structure (Figure 2). The reduced spatial extent of the larger particle trajectories, which is integrally related to hindered particle dynamics, will be discussed later in the paper.

To characterize the void space morphology, we used confocal laser scanning microscopy to image a
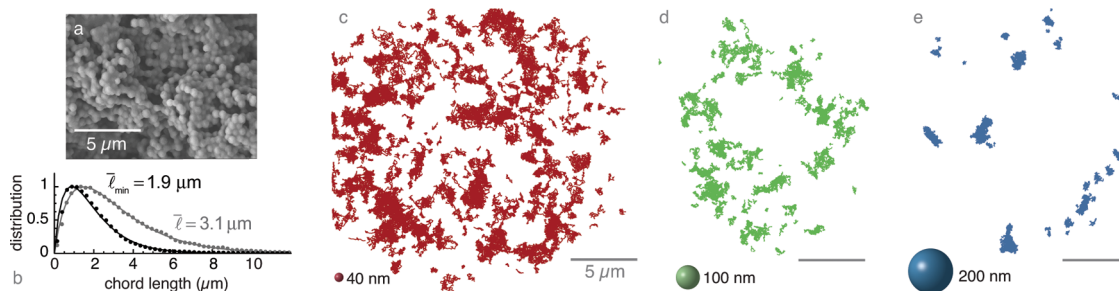
Figure 2. Single particle trajectories confined to the void space. (a) SEM image of the porous network with porosity $\phi = 0.50 \pm 0.07$. (b) The chord length (gray) and confinement length (black) distributions measured in the void space (symbols). The mean chord length $\overline{l}$ (i.e., mean void size) and the mean confinement length, $\overline{l}_{min}$, obtained from a fit to the k-Gamma distribution (solid line, see Methods S1 of the Supporting Information), are annotated. Displayed at the same spatial scale as the SEM image (a) are trajectories of 40 nm (c), 100 nm (d) and 200 nm (e) particles. The absence of trajectories near the perimeter in (c), (d) and (e) is the result of different illuminated areas in the experiments.

three-dimensional section of the permeating liquid, which was fluorescently dyed. The confocal data revealed a disordered void network similar to that exposed in the SEM images, albeit at lower resolution (Figure S1 of the Supporting Information). Using the two-dimensional confocal sections, we measured the void volume fraction $\phi = 0.50 \pm 0.07$ (i.e., porosity), the distribution of chord lengths (Figure 2b),[38] which characterize the size of the void spaces, and the distribution of minimum chord lengths (i.e., confinement lengths), which characterize the length scale of maximum confinement (Methods S1 and Figure S1 of the Supporting Information). An independent measure of porosity based on the change in sample mass upon saturating with fluid, $\phi = 0.52 \pm 0.02$, agreed well with the confocal value.

Hydrodynamic Interactions and Spatially Heterogeneous Diffusion. We expected the confined particles to diffuse more slowly due to geometric confinement by the solid matrix, but we found that hydrodynamic interactions between the particles and pore walls had a more significant influence on particle mobility. At even the shortest times accessible experimentally, particle motion was slowed compared to the unconfined bulk (Figure 3). At short times, based on the particles' bulk diffusion coefficients (Table S1 of the Supporting Information), we expect few collisions between the particles and the pore walls. In 0.1 s, on average, the 40, 100, and 200 nm particles moved 187 nm, 122 and 89 nm respectively, which was an order of magnitude less than the average void size, but the diffusion coefficients were reduced by 50, 49 and 60%, respectively (Figure 3 and Table S1 of the Supporting Information).

To isolate the influence of geometric confinement on particle dynamics, we performed lattice Monte Carlo simulations of random walks within the imaged void space (Methods S2 of the Supporting Information). The simulations, which did not include hydrodynamic effects, produced only a minor reduction in the diffusion coefficient at short times (solid lines in
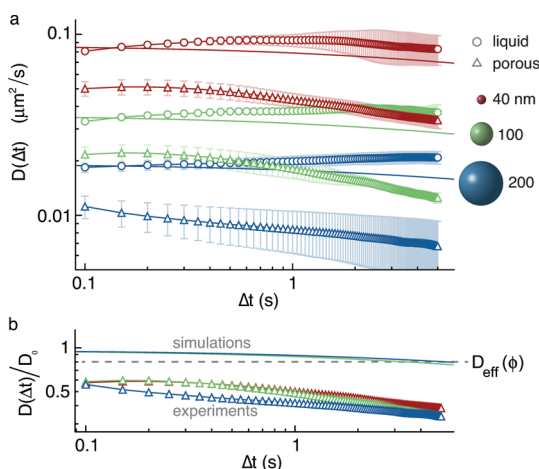

Figure 3. Confinement leads to a decreasing time-dependent diffusion coefficient. (a) The time-dependent diffusion coefficient, $D(\Delta t) = \langle r^2 \rangle / 4\Delta t$, for each of the particle sizes, in unconfined bulk liquid and confined within the porous network. The lines connecting the symbols are a guide to the eye. Error bars are the standard deviation between data from $n \geq 3$ porous samples or $n = 5$ subsets of data in the unconfined bulk. Solid lines are results from random walk simulations within the porous voids as described in the text. (b) The time-dependent diffusion coefficient normalized by the bulk diffusion coefficient D_0 and an analytical prediction for the limiting diffusion coefficient based on the porosity of the medium[39] (dashed line).

Figure 3). The experimentally observed reduction in confined diffusion coefficient was also much greater than analytical predictions for diffusion in the presence of circular obstacles in the absence of hydrodynamics.[39] For a porosity of $\phi = 0.5$, the effective long-time diffusion coefficient is predicted to be $D_{eff}(\phi) = D_0/(1 + 0.5(1 - \phi)) = 0.8(D_0)$, where D_0 is the unconfined bulk diffusion coefficient (Figure 3b).[39] Taking into account higher order correlations in the porous structure further reduces the effective diffusion coefficient, $D_{eff}(\phi = 0.5) \sim 0.75(D_0)$.[39] This reduction is similar to what we observed in the simulations (Figure 3) at long time intervals, but the predicted values remained much greater than the experimentally measured values of $\sim 0.5D_0$. We attribute this greater than expected

reduction in diffusion coefficient to the presence of long-range hydrodynamic damping of confined particle motion.

Hydrodynamic interactions increase the frictional damping of particle motion, and expressions have been developed to estimate the magnitude of hydrodynamic damping in simple geometries, such as cylinders and near flat walls.[40] To estimate the hydrodynamic drag on the particles confined in the heterogeneous void space, we used the superposition approach shown by Imperio *et al.* to accurately describe hydrodynamic damping in microcavities.[40] We approximated confinement with a cubic box of side length h, and calculated the average hydrodynamic drag on a particle of radius R by summing over the contributions from each of the six walls (Methods S3 of the Supporting Information). We then averaged over different confinement lengths h, given by the experimental distribution of minimum chord lengths (Figure 2b). Using this model, we expected a reduced diffusion coefficient of 0.72, 0.57, and 0.43 for the 40 nm, 100 and 200 nm particles. While this calculation provided significantly improved agreement with the measurements, the estimates were systematically higher than the experimental values of 0.50, 0.51 and 0.40, and the difference systematically increased with decreasing particle size. A possible explanation for this discrepancy is that the limited confocal resolution (~200 nm) produced an overestimate of the mean confinement length, and limited our ability to characterize some void spaces accessible to the smallest particles. The significance of hydrodynamic interactions in determining the reduced diffusion of confined particles has been observed in other experiments at large length scales.[14,15] Our results highlight the importance of hydrodynamics at subpore length scales, and short time scales, where geometric obstruction has less influence.

Although the tracer particles varied in size by almost an order of magnitude, the normalized time-dependent diffusion coefficient, $D(\Delta t)/D_0$, behaved similarly in all of the experiments (Figure 3b). (The similar time-dependence was also reflected in the temporal scaling of the mean square displacement, *i.e.*, the anomalous diffusion exponent (Figure S2 of the Supporting Information).) This was probably due to the broad distribution of void sizes (Figure 2b). It has been shown that diffusion in highly disordered structures is insensitive to particle size, because particles, regardless of size, experience similar confinement.[41] A greater dependence of diffusion on particle size is expected in ordered porous structures, and was observed in a number of experiments.[17,35] Interestingly, with ordered cylindrical obstacles, the reduction in diffusion was more modest than we observed,[35] and might reflect the difference in hydrodynamic interactions with obstacles of different dimensionality (*i.e.*, quasi
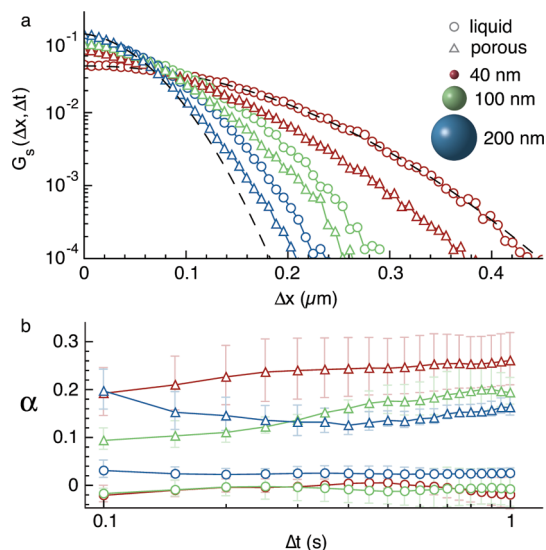

Figure 4. Distributions of particle displacements are non-Gaussian when particles are confined in the porous medium. (a) Displacement probability distributions for each particle size confined to the porous medium and in unconfined bulk liquid, calculated for $\Delta t = 0.1$ s. The dashed lines are Gaussian fits to the porous 200 nm data and unconfined liquid 40 nm data. **(b)** The non-Gaussian parameter $\alpha = \langle \Delta x^4 \rangle / [3\langle \Delta x^2 \rangle^2] - 1$ as a function of lag time ($\alpha = 0$ for a Gaussian). The lines connecting the symbols are a guide to the eye. Error bars are the standard deviation between data from $n \geq 3$ porous samples or $n = 5$ subsets of data in the unconfined bulk.

1D cylinders *versus* extended 3D objects).[42] Porous materials are generally categorized by a few structural classes,[9] such as fibrous gels and packed fiber filters or extended three-dimensional obstacles, like the material we studied, so the influence of hydrodynamics may be qualitatively different in these different cases.

Non-Gaussian Displacements. The influence of hydrodynamic interactions was also evident in the probability distributions of particle displacements (G_s), which were non-Gaussian over the full experimental range of time intervals (Figure 4b). Even at the shortest experimental time scales, when there were few direct particle−wall collisions and the mean square displacements were approximately Fickian (*i.e.*, $D(\Delta t) =$ constant (Figure 3)), the displacement distributions decayed more slowly than a Gaussian. Although the smallest particles appeared to be the most non-Gaussian (Figure 4b), the noise in the measurement prevented us from assigning physical significance to the differences between particle sizes. (The noise, which is related to dividing two large, approximately equal numbers, also limited the time range of the measurement.) In the heterogeneous void space of the porous medium, we expect that hydrodynamic particle-wall interactions would give rise to a spatially varying diffusion coefficient that would depend on the local void size and position of the particle within the void. In fact, spatial maps of mobility and trajectory based analysis revealed spatially dependent mobility

and increasing heterogeneity with increasing particle size (Figure S4 and Discussion S1 of the Supporting Information). As a result, the ensemble displacement distributions would reflect a collection of local diffusive processes, each with a corresponding Gaussian of different variance.

The same sum-of-Gaussians interpretation has been used previously to explain diffusion in colloidal systems,[43] but in that case diffusion was temporally heterogeneous rather than spatially heterogeneous as observed here. Spatially dependent diffusion processes have also been investigated theoretically[44,45] and observed in biological systems.[46] Pursuing this line of reasoning, we modeled the experimental displacement distributions as a weighted sum of Gaussians, $G_s(\Delta x) = \int p(\Delta x, D) w(D) \, dD$, where $p(\Delta x, D)$ are elementary Gaussians corresponding to a diffusion coefficients D, and $w(D)$ are the weights. Again using the superposition model for hydrodynamic drag in microcavities of size h,[40] and the experimentally measured distribution of confinement lengths $f(l_{min})$ (Figure 2b), we numerically calculated $G_s(\Delta x) = \int p(\Delta x, D_{h=l_{min}}) f(l_{min}) \, dD_{l_{min}}$. With no adjustable parameters, aside from a multiplicative constant, we found $G_s(\Delta x)$ to be non-Gaussian, but quantitative agreement with the experimental data was poor (Figure S5 of the Supporting Information). This may reflect the heavily simplified model used to estimate hydrodynamic drag, and we would expect better agreement if we treated the hydrodynamics in the true disordered void space, but to our knowledge, there are no simple expressions for hydrodynamics under such general conditions.

The non-Gaussian and non-Fickian diffusion that we observed is expected to be transient. At long times, after the particles have fully sampled the distribution of diffusion coefficients $w(D)$ and the distribution of void sizes, the dynamics should converge to normal Gaussian diffusion with reduced mobility governed by the effective medium of the porous network. This raises two questions: at what time and length scales will diffusion become homogeneous and in what scenarios is it important that the dynamics are heterogeneous and anomalous at intermediate times? Regarding the first question, we expected a transition to normal diffusion at length scales greater than the correlation length of the void space, $r \gg \xi$, which in our porous sample was similar to the average void size, $\xi \sim 3.1 \, \mu$m (Figure S6 of the Supporting Information). The length scale at which this transition occurs depends on the structure of the void space; in particular for a highly disordered space, the transition may not occur until reaching a length scale an order of magnitude larger than the correlation length.[47] In our case, this would be approximately 30 μm, which is approaching the thickness of the porous film (Figure 1a), and would correspond to a time scale on the order of hours. Thus, it might be important to consider diffusion heterogeneity

when the physical dimensions of the porous material (e.g., particle diameter or film thickness) approach the correlation length of the porous network. Pore-scale heterogeneity would also be important in the context of confined transport-limited reactions and signaling when sources and sinks are spatially localized (e.g., cells immobilized in a porous scaffold) because local reaction rates would be highly heterogeneous. Even the average reaction rate can depend on pore-scale details, because they modify the statistical properties of the diffusing reactant.[24] The influence of heterogeneity would be even more significant in cases where reactive/binding sites themselves are spatially correlated because transport between sites might be different than the average bulk transport rate. It has also been shown that with increasing confinement, reaction kinetics depend crucially on the spatial correlation of the reactant and reactive site, giving rise to so-called "geometry controlled kinetics".[25]

Transport-Dependent Pore Accessibility. We return now to the discussion of the size-dependent accessibility of the void space (Figure 2c,d,e). We first address possible equilibrium mechanisms before considering kinetic mechanisms related to the confined hydrodynamics, which we ultimately determined were responsible for the observed void accessibility. The particles were introduced into the void space along with the permeating liquid, so the initial particle configuration may not have been at equilibrium. Therefore, the focus of this discussion is on the extent to which particles, once in the voids, explored the accessible volume. Surprisingly, only the smallest 40 nm particles explored a sizable fraction of the void space, despite the fact that the mean void size, $\sim 3.1 \, \mu$m, was an order of magnitude larger than even the largest 200 nm particle (Figure 2). The larger 100 and 200 nm particles accessed systematically lower fractions of the void space. This was true even when we normalized by the total number of observations (Figure S7 of the Supporting Information), which accounts for differences in statistical sampling related to the slower diffusion of larger particles.

One possible explanation for the surprisingly small accessible volume is that there were long-range repulsive interactions between the particles and pore walls, which reduced the effective void size. We believe that this is unlikely because in the absence of surfactant, there was strong attraction between the particles and solid matrix and it is unlikely that the addition of nonionic surfactant changed the attractive interaction into a micron length scale repulsive interaction. We also used the diffusion coefficient in pure liquid to estimate the hydrodynamic diameters of the particles based on the Stokes−Einstein equation, $D = kT/6\pi\eta R$, and the estimated sizes (62, 126, and 234 nm) were systematically larger than the nominal sizes provided by the manufacturer (40, 100, and 200 nm) but still

much less than the typical void size. Another possible explanation for the limited void accessibility is that the connectivity of the void space was such that large voids were only connected *via* a small number of narrow passages. Void connectivity is not captured by the distribution of void sizes, so we investigated this possibility using confocal volumes and the simulated random walks. After thresholding the confocal volumes to identify the void space, we found that the void space was fully connected (*i.e.*, percolating) by passages larger than the 100 nm dimensions of the confocal voxels. We also simulated random walks within the three-dimensional void space and we found that even for 200 nm particles, the void space was fully accessible (Figure S8 of the Supporting Information). The random walks were simulated on the three-dimensional lattice defined by the confocal volumes, where during each simulation time step (determined by the particle's diffusion coefficient) the particle was allowed to execute a nearest neighbor step onto lattice sites corresponding to void and not matrix. (Additional simulation details are in Discussion S2 of the Supporting Information.)

Having ruled out equilibrium explanations of the size-dependent accessibility of the void space, we considered possible kinetic mechanisms involving hindered transport. The initial random walk simulations confirmed the connectivity of the void space, but they did not account for the spatially dependent hydrodynamics or the finite duration of the experiments. It may be that the hindered particle diffusion prevented particles from fully exploring the void space within the approximately 1 h time scale of the experiments. To test this possibility, we first simulated random walks in which we accounted for the average hydrodynamically reduced pore diffusion and the finite duration of the experiments (Figure 5a). This was implemented by adjusting the waiting time between each simulated lattice displacement and limiting the total length of the simulated trajectories. In this case, the simulated trajectories accessed a smaller fraction of the void space than before (Figure S8 of the Supporting Information), but still the simulated walks explored more of the voids than the experimental trajectories (Figure S7 of the Supporting Information). However, when we simulated random walks in the presence of a spatially dependent diffusion coefficient defined by the hydrodynamics, the walks accessed a much smaller volume (Figure 5b). In this case, we implemented a variable waiting time on each lattice site, which was determined by the estimated local hydrodynamic drag. These data suggest that the void accessibility was dependent on the full heterogeneous hydrodynamic details of the confined particle diffusion. Accounting only for the average reduced mobility was not enough because a gradient in diffusion coefficient, in this case the result of varying hydrodynamics,
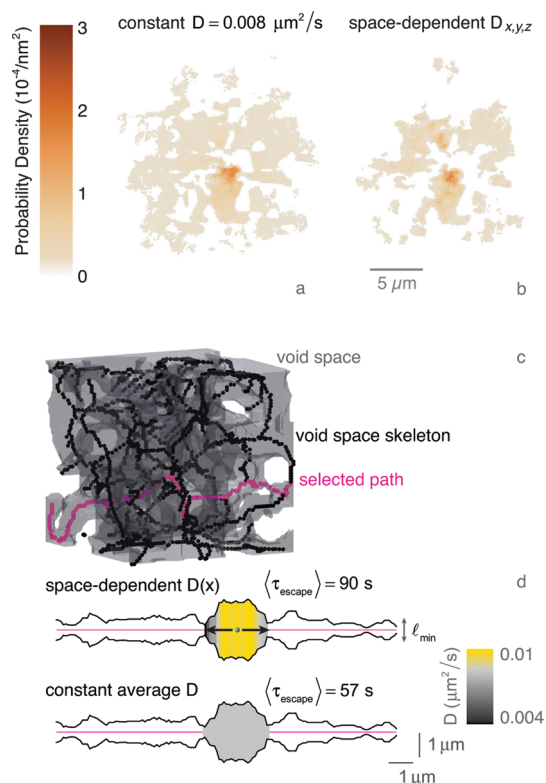

Figure 5. Space-dependent mobility slows particle exploration of the void space. (a) The spatial probability density of observing a simulated random walk within the imaged void space, taking into account the average reduced particle diffusion and (b) the spatially dependent diffusion coefficient. (c) The morphological skeleton, or medial axis, of a portion of the imaged void space showing the selected path along the skeleton used for further analysis. (d) The varying confinement length (black traces) along the selected path created a position dependent diffusion coefficient. Simulating diffusion along the path with an inhomogeneous diffusion coefficient resulted in a larger mean escape time from the indicated void compared to the case where the particle experienced a constant average diffusion coefficient.

enforces a local drift in the particle displacements.[48,49] This in turn increases the time for a particle to escape from a confining void. To illustrate this more clearly, we extracted a random path through the imaged void space and measured the confinement length as a function of position along the path (Figure 5c). We then simulated diffusion along this one-dimensional path with either a position dependent diffusion coefficient given by the local confinement length, or a constant average diffusion coefficient. We found that the mean escape time from a particular void was ∼60% greater with a spatially dependent diffusion coefficient compared to a constant average diffusion coefficient (Figure 5d). This means that the rate at which particles explore the void space is dependent on the full description of locally varying hydrodynamics.

Our data suggest that the limited accessibility of the void space was due to spatially dependent hydrodynamic damping of particle motion and details of the pore structure. Simple steric interactions or the

average reduction in particle mobility alone were not enough to explain the observed void accessibility. The interpretation that transport controlled the accessibility of the void space is at odds with the typical equilibrium interpretation of size-exclusion chromatography, but there is still ongoing debate regarding the underlying mechanism of size-exclusion.[2,50] Our interpretation also implies that the observed size-exclusion was not fundamental to the porous system we studied, but rather was a function of the time scale of the observation. This highlights the importance of hydrodynamics and pore structure in determining the accessible volume at a particular time scale of interest. The important point is that a simple comparison of solute size and average pore size may not be enough to determine the accessible pore volume and the time scale for full exploration of the void space might be much longer than anticipated.

CONCLUSION

We tracked the motion of individual nanoparticles as they diffused within the disordered void space of a three-dimensional porous medium. To image particle motion deep within a porous material of moderate porosity, it was necessary to permeate the pores with an index matching liquid. The method we developed, which uses a high refractive index polar liquid, will enable studies of many new materials, which go beyond the high porosity or low refractive index materials studied in the past. For example, many porous polymers of technological interest, such as poly(vinylidene fluoride), nitrocellulose and poly(L-lactic acid) could be investigated with this method. Using the method to track the motion of nanoparticles in the liquid filled voids of a porous polymer, we observed significant hydrodynamic damping of particle motion that gave rise to heterogeneous and spatially dependent dynamics. Even at length scales much less than the average void size, particle diffusion was reduced compared to the unconfined case. These results highlight the importance of hydrodynamics in confined diffusion processes. In the context of porous diffusion models based on steric confinement, inclusion of hydrodynamics would not only dampen motion, but also introduce an additional degree of heterogeneity due to subpore variations in diffusion coefficient. The time scale of the heterogeneity, characterized by the non-Gaussian statistics, would also increase with increasing fluid viscosity.

We also observed unexpectedly strong size-exclusion of the particles within the heterogeneous void space. We attributed the limited void accessibility to a kinetic mechanism of restricted transport caused by the spatial dependence of the hydrodynamic drag. This could be significant in heterogeneous catalysis applications where unexpected restriction of pore access could make a process transport-limited that was expected to be reaction limited. It also means that separation processes might become flow-rate dependent at lower fluid velocities than expected, and because the kinetics of void access depend on hydrodynamics, the separation would also depend on fluid viscosity. Kinetic barriers that slow the diffusive spreading of particles would also influence the compactness of a search process and the resulting reaction kinetics.[24] It has been shown, for example, that as the void escape time increases (e.g., Figure 5d) and the total diffusion coefficient decreases, the reaction rate may be higher than the classical prediction because the particles more thoroughly explore the volume.[24] In general, our results suggest that a simple comparison of particle and pore sizes may overestimate the particle mobility and accessible volume of the pore network, whether it be a chromatographic material, drug-laden particle, or the interior of a cell.

Our results leave several questions unanswered. For example, how do attractive particle−pore wall interactions influence dynamics and transport dependent reactions? In particular, will it be possible to distinguish the contributions of attractive interactions, hydrodynamics and confinement in systems where all three are present? Using the approach that we presented here, we believe that it will be possible to answer these questions and further understand and control porous diffusion.

METHODS

Porous Polymer Synthesis. The porous polymer films were synthesized using *in situ* photopolymerization during the forced evaporation of an organic solvent (or mixture).[51] The solution consisted of a Norland optical adhesive 65 precursor (NOA65, Norland Products) and a cosolvent of carbon disulfide (CS$_2$, ACS reagent grade, Sigma-Aldrich) and isopropanol (IPA, certified ACS plus grade, Fisher Scientific) with a formulation (by mass) of NOA65/CS$_2$/IPA = 10/40/50%. Note that IPA is a nonsolvent for NOA65. To prepare this solution, NOA65 was first added to a vial containing IPA and then CS$_2$ was slowly titrated to prevent any precipitation. The film-forming process was carried out in a home-built reaction chamber that allows variable purging with N$_2$ to both remove the O$_2$ that is detrimental to

some photo-cross-linking reaction and to control the evaporation rate of the solvent. For each film preparation, the N$_2$ stream was purged for at least 5 min to saturate the reaction chamber prior to the solution deposition. Subsequently, a 100 μL solution drop was deposited onto the cover glass (untreated and air blown for 1 min) by a micropipette and immediately exposed to UV radiation at ~50 mW/cm^2 for 5 min, by use of an OmniCure S2000 spot curing system with a notch filter (320−500 nm) and a collimating kit. A field emission scanning electron microscope (FE-SEM) (JEOL JSM-7401F) was used to characterize the cross-sectional morphology of the as-prepared films.

Imaging Nanoparticle Diffusion. We imaged the diffusion of submicron colloidal spheres suspended in a liquid that permeated the void space of a porous polymer film. The colloid spheres were fluorescent polystyrene of three different

diameters: 40 nm (dark red, F-8789, Life Technologies) 100 nm (orange, F-8800, Life Technologies) and 200 nm (yellow-green, F-8811, Life Technologies). The particles were dispersed in a 5:1 mixture of thiodiethanol (TDE, Sigma-Aldrich) and Triton X-100 (Sigma-Aldrich), by volume. This suspending liquid matched the refractive index of the polymer matrix ($n = 1.52$) and prevented particle binding to the pore walls. The particle concentration was sufficiently low (volume fraction $10^{-4} < \phi < 10^{-6}$) to avoid particle−particle interactions and allow identification of individual particles in the single-particle tracking experiments.

The prepared polymer films were first soaked in isopropanol (Sigma-Aldrich) for 48 h. Before an experiment, the polymer sample was blown dry with nitrogen and then sealed in a vacuum desiccator for approximately 1 h. Approximately 50 μL of fluorescent particle suspension was then pipetted onto the top surface of the porous film, allowed to infiltrate the pores and saturate the film ($\sim$10 min), and then equilibrated for 1 h.

After saturating the void space with the fluorescent particle suspension, the porous samples were imaged using a modified epifluorescence microscope (TE-2000, Nikon). Fluorescence excitation was provided by one of three lasers, depending on the particle being imaged: a 491 or 532 nm diode-pumped solid state laser (Cobolt AB), or a 640 nm diode-pumped solid state laser (Crystal Laser). Excitation light was delivered and the fluorescence emission collected by a 60×, NA = 1.2, water-immersion objective (Nikon). The emitted light was passed through a 1.5× relay lens and imaged on an electron-multiplying CCD camera (Andor iXon3), resulting in 145 nm/pixel at the image plane. We imaged particle diffusion 20−30 μm above the polymer-glass interface, near the midplane of the porous film, at a frame rate of 20 Hz for a total of $\sim$1 h.

To identify and track the motion of individual particles in the image sequences, we used custom software that implemented the radial symmetry algorithm.[52] Subpixel particle positions were linked frame-to-frame into two-dimensional trajectories using a nearest neighbor distance threshold of $R = 1.25, 1.5,$ and 2.0 pixels for the 200, 100, and 40 nm particles, respectively. In some samples, a small number of trajectories ($\sim$10) appeared immobilized, and although they made up a small fraction of the total trajectories observed ($\sim$0.1%), they significantly influenced the measured dynamics. Therefore, trajectories with an end-to-end distance <60 nm were excluded from further analysis.

Conflict of Interest: The authors declare no competing financial interest.

REFERENCES AND NOTES

1. Shannon, M. A.; Bohn, P. W.; Elimelech, M.; Georgiadis, J. G.; Marinas, B. J.; Mayes, A. M. Science and Technology for Water Purification in the Coming Decades. *Nature* **2008**, *452*, 301–310.

2. Berek, D. Size Exclusion Chromatography—a Blessing and a Curse of Science and Technology of Synthetic Polymers. *J. Sep. Sci.* **2010**, *33*, 315–335.

3. Ma, P. X. Scaffolds for Tissue Fabrication. *Mater. Today* **2004**, *7*, 30–40.

4. Zhang, Y. S.; Choi, S.-W.; Xia, Y. Inverse Opal Scaffolds for Applications in Regenerative Medicine. *Soft Matter* **2013**, *9*, 9747–9754.

5. Minchinton, A. I.; Tannock, I. F. Drug Penetration in Solid Tumours. *Nat. Rev. Cancer* **2006**, *6*, 583–592.

6. Berlin, J. M.; Yu, J.; Lu, W.; Walsh, E. E.; Zhang, L.; Zhang, P.; Chen, W.; Kan, A. T.; Wong, M. S.; Tomson, M. B. Engineered Nanoparticles for Hydrocarbon Detection in Oil-Field Rocks. *Energy Environ. Sci.* **2011**, *4*, 505–509.

7. Ehtesabi, H.; Ahadian, M. M.; Taghikhani, V.; Ghazanfari, M. H. Enhanced Heavy Oil Recovery in Sandstone Cores Using TiO₂ Nanofluids. *Energy Fuels* **2013**, *28*, 423–430.

8. Kim, I. C.; Torquato, S. Diffusion of Finite-Sized Brownian Particles in Porous Media. *J. Chem. Phys.* **1991**, *96*, 1498.

9. Novikov, D. S.; Jensen, J. H.; Helpern, J. A.; Fieremans, E. Revealing Mesoscopic Structural Universality with Diffusion. *Proc. Natl. Acad. Sci. U. S. A.* **2014**, *111*, 5088–5093.

10. Bauer, M.; Godec, A.; Metzler, R. Diffusion of Finite-Size Particles in Two-Dimensional Channels with Random Wall Configurations. *Phys. Chem. Chem. Phys.* **2014**, *16*, 6118–6128.

11. Levesque, M.; Bénichou, O.; Rotenberg, B. Molecular Diffusion between Walls with Adsorption and Desorption. *J. Chem. Phys.* **2013**, *138*, 034107.

12. Höfling, F.; Franosch, T.; Frey, E. Localization Transition of the Three-Dimensional Lorentz Model and Continuum Percolation. *Phys. Rev. Lett.* **2006**, *96*, 165901.

13. Bauer, M.; Metzler, R. Collective Dynamics Effect Transient Subdiffusion of Inert Tracers in Flexible Gel Networks. *New J. Phys.* **2014**, *16*, 092002.

14. Kluijtmans, S. G.; de Hoog, E. H.; Philipse, A. P. Self-Diffusion of Charged Colloidal Tracer Spheres in Transparent Porous Glass Media: Effect of Ionic Strength and Pore Size. *J. Chem. Phys.* **1998**, *108*, 7469–7477.

15. Kluijtmans, S. G.; Philipse, A. P. First *In Situ* Determination of Confined Brownian Tracer Motion in Dense Random Sphere Packings. *Langmuir* **1999**, *15*, 1896–1898.

16. Beschieru, V.; Rathke, B.; Will, S. Particle Diffusion in Porous Media Investigated by Dynamic Light Scattering. *Microporous Mesoporous Mater.* **2009**, *125*, 63–69.

17. Raccis, R.; Nikoubashman, A.; Retsch, M.; Jonas, U.; Koynov, K.; Butt, H.-J. r.; Likos, C. N.; Fytas, G. Confined Diffusion in Periodic Porous Nanostructures. *ACS Nano* **2011**, *5*, 4607–4616.

18. Karger, J.; Binder, T.; Chmelik, C.; Hibbe, F.; Krautscheid, H.; Krishna, R.; Weitkamp, J. Microimaging of Transient Guest Profiles to Monitor Mass Transfer in Nanoporous Materials. *Nat. Mater.* **2014**, *13*, 333–343.

19. Cherdhirankorn, T.; Retsch, M.; Jonas, U.; Butt, H.-J.; Koynov, K. Tracer Diffusion in Silica Inverse Opals. *Langmuir* **2010**, *26*, 10141–10146.

20. Saxton, M. J. Wanted: A Positive Control for Anomalous Subdiffusion. *Biophys. J.* **2012**, *103*, 2411–2422.

21. Höfling, F.; Franosch, T. Anomalous Transport in the Crowded World of Biological Cells. *Rep. Prog. Phys.* **2013**, *76*, 046602.

22. Schuss, Z.; Singer, A.; Holcman, D. The Narrow Escape Problem for Diffusion in Cellular Microdomains. *Proc. Natl. Acad. Sci. U. S. A.* **2007**, *104*, 16098–103.

23. Condamin, S.; Tejedor, V.; Voituriez, R.; Bénichou, O.; Klafter, J. Probing Microscopic Origins of Confined Subdiffusion by First-Passage Observables. *Proc. Natl. Acad. Sci. U. S. A.* **2008**, *105*, 5675.

24. Li, R.; Fowler, J. A.; Todd, B. A. Calculated Rates of Diffusion-Limited Reactions in a Three-Dimensional Network of Connected Compartments: Application to Porous Catalysts and Biological Systems. *Phys. Rev. Lett.* **2014**, *113*, 028303.

25. Bénichou, O.; Chevalier, C.; Klafter, J.; Meyer, B.; Voituriez, R. Geometry-Controlled Kinetics. *Nat. Chem.* **2010**, *2*, 472–477.

26. Metzler, R.; Jeon, J.-H.; Cherstvy, A. G.; Barkai, E. Anomalous Diffusion Models and Their Properties: Non-Stationarity, Non-Ergodicity, and Ageing at the Centenary of Single Particle Tracking. *Phys. Chem. Chem. Phys.* **2014**, *16*, 24128–24164.

27. Cherstvy, A. G.; Chechkin, A. V.; Metzler, R. Particle Invasion, Survival, and Non-Ergodicity in 2d Diffusion Processes with Space-Dependent Diffusivity. *Soft Matter* **2014**, *10*, 1591–1601.

28. Burada, P. S.; Hänggi, P.; Marchesoni, F.; Schmid, G.; Talkner, P. Diffusion in Confined Geometries. *ChemPhysChem* **2009**, *10*, 45–54.

29. Hänggi, P.; Marchesoni, F. Artificial Brownian Motors: Controlling Transport on the Nanoscale. *Rev. Mod. Phys.* **2009**, *81*, 387.

30. Kirstein, J.; Platschek, B.; Jung, C.; Brown, R.; Bein, T.; Brauchle, C. Exploration of Nanostructured Channel Systems with Single-Molecule Probes. *Nat. Mater.* **2007**, *6*, 303–310.

31. Zurner, A.; Kirstein, J.; Doblinger, M.; Brauchle, C.; Bein, T. Visualizing Single-Molecule Diffusion in Mesoporous Materials. *Nature* **2007**, *450*, 705–8.

32. Wong, I.; Gardel, M.; Reichman, D.; Weeks, E. R.; Valentine, M.; Bausch, A.; Weitz, D. Anomalous Diffusion Probes Microstructure Dynamics of Entangled F-Actin Networks. *Phys. Rev. Lett.* **2004**, *92*, 178101.

33. Lee, C. H.; Crosby, A. J.; Emrick, T.; Hayward, R. C. Characterization of Heterogeneous Polyacrylamide Hydrogels by Tracking of Single Quantum Dots. *Macromolecules* **2014**, *47*, 741–749.

34. Guan, J.; Wang, B.; Granick, S. Even Hard-Sphere Colloidal Suspensions Display Fickian yet Non-Gaussian Diffusion. *ACS Nano* **2014**, *8*, 3331–3336.

35. He, K.; Babaye Khorasani, F.; Retterer, S. T.; Thomas, D. K.; Conrad, J. C.; Krishnamoorti, R. Diffusive Dynamics of Nanoparticles in Arrays of Nanoposts. *ACS Nano* **2013**, *7*, 5122–5130.

36. Eral, H.; Oh, J.; Van Den Ende, D.; Mugele, F.; Duits, M. Anisotropic and Hindered Diffusion of Colloidal Particles in a Closed Cylinder. *Langmuir* **2010**, *26*, 16722–16729.

37. Staudt, T.; Lang, M. C.; Medda, R.; Engelhardt, J.; Hell, S. W. 2,2′-Thiodiethanol: A New Water Soluble Mounting Medium for High Resolution Optical Microscopy. *Microsc. Res. Tech.* **2007**, *70*, 1–9.

38. Stoeckel, D.; Kübel, C.; Hormann, K.; Höltzel, A.; Smarsly, B. M.; Tallarek, U. Morphological Analysis of Disordered Macroporous−Mesoporous Solids Based on Physical Reconstruction by Nanoscale Tomography. *Langmuir* **2014**, *30*, 9022–9027.

39. Liasneuski, H.; Hlushkou, D.; Khirevich, S.; Höltzel, A.; Tallarek, U.; Torquato, S. Impact of Microstructure on the Effective Diffusivity in Random Packings of Hard Spheres. *J. Appl. Phys.* **2014**, *116*, 034904.

40. Imperio, A.; Padding, J. T.; Briels, W. Diffusion of Spherical Particles in Microcavities. *J. Chem. Phys.* **2011**, *134*, 154904.

41. Saxton, M. J. Lateral Diffusion in an Archipelago. Dependence on Tracer Size. *Biophys. J.* **1993**, *64*, 1053–1062.

42. Clague, D. S.; Phillips, R. J. Hindered Diffusion of Spherical Macromolecules through Dilute Fibrous Media. *Phys. Fluids* **1996**, *8*, 1720–1731.

43. Wang, B.; Anthony, S. M.; Bae, S. C.; Granick, S. Anomalous yet Brownian. *Proc. Natl. Acad. Sci. U. S. A.* **2009**, *106*, 15160–15164.

44. Cherstvy, A. G.; Metzler, R. Population Splitting, Trapping, and Non-Ergodicity in Heterogeneous Diffusion Processes. *Phys. Chem. Chem. Phys.* **2013**, *15*, 20220–20235.

45. Massignan, P.; Manzo, C.; Torreno-Pina, J.; García-Parajo, M.; Lewenstein, M.; Lapeyre, G., Jr. Non-Ergodic Subdiffusion from Brownian Motion in an Inhomogeneous Medium. *Phys. Rev. Lett.* **2014**, *112*, 150603.

46. English, B. P.; Hauryliuk, V.; Sanamrad, A.; Tankov, S.; Dekker, N. H.; Elf, J. Single-Molecule Investigations of the Stringent Response Machinery in Living Bacterial Cells. *Proc. Natl. Acad. Sci. U. S. A.* **2011**, *108*, E365–E373.

47. Saxton, M. J. Lateral Diffusion and Aggregation. A Monte Carlo Study. *Biophys. J.* **1992**, *61*, 119–128.

48. Lançon, P.; Batrouni, G.; Lobry, L.; Ostrowsky, N. Drift without Flux: Brownian Walker with a Space-Dependent Diffusion Coefficient. *Europhys. Lett.* **2001**, *54*, 28.

49. Marchesoni, F. Drift in Diffusion Gradients. *Materials* **2013**, *6*, 3598–3609.

50. Wang, Y.; Teraoka, I.; Hansen, F. Y.; Peters, G. n. H.; Hassager, O. A Theoretical Study of the Separation Principle in Size Exclusion Chromatography. *Macromolecules* **2010**, *43*, 1651–1659.

51. Wang, L.; Zhang, Z.; Ding, Y. Photocrosslinking-Induced Phase Separation in Evaporative Solvents: Formation of Skin Layers and Microspheres. *Soft Matter* **2013**, *9*, 4455–4463.

52. Parthasarathy, R. Rapid, Accurate Particle Tracking by Calculation of Radial Symmetry Centers. *Nat. Methods* **2012**, *9*, 724–726.